# Evaluating the Effectiveness of ICESat-2 ATL03 Data for Georeferencing Satellite Images

Heyi Li [1], Wei Qin [2, *], Dan Zhou [1], Quan Jing [1], Xiao Zhang [3], Pengjie Tao [2, 4]

[1] Institution of Remote Sensing Satellite, Chinese Academy of Space Technology, Beijing 100094, China - hey1li@126.com, 67005202@qq.com, springf6@hotmail.com,
[2] School of Remote Sensing and Information Engineering, Wuhan University, Wuhan 430079, China - wei-qin@whu.edu.cn, pjtao@whu.edu.cn
[3] CCCC Second Highway Consultants Co. Ltd, Wuhan 430056, China - xiaozhxr@163.com
[4] Hubei Luojia Laboratory, Wuhan 430079, China

**Keywords:** ICESat-2 ATL03 data, Geometric accuracy assessment, Satellite images georeferencing, Digital control photo.

**Abstract**

ICESat-2 laser points, as a kind of public geographic data, have high ranging accuracy and have great potential in improving the geometric positioning accuracies of satellite images. This paper aims to evaluate the effectiveness of ICESat-2 ATL03 data for georeferencing satellite image. Our study combines ATL03 laser points with an image basemap processed using open-source data positioning to construct digital control photo (DCP), facilitating the rapid transformation of laser points into laser control points for image georeferencing. Through a comprehensive analysis involving comparison with traditional georeferencing methods using ground control points (GCPs), our findings indicate a significant enhancement in accuracy and efficiency in georeferencing, showcasing the potential of ICESat-2 data in improving the quality and reliability of remote sensing images. Experiments using the extracted laser points and GeoEye-1 images to construct DCP for georeferencing IKONOS images in Hobart, Australia demonstrate that the proposed method improved the horizontal accuracy from 2.33 meters to 0.97 meters and the vertical accuracy from 3.44 meters to 0.59 meters, compared to the georeferencing method without GCPs.

## 1. Introduction

Geometric correction of images is a fundamental technology for remote sensing images (Gonçalves et al., 2009). By eliminating the systematic geometric errors of remote sensing images, we can improve the geometric accuracies and reliabilities of the images, thus restoring the true geometric shapes of the scenes (Dave et al., 2015). This process is crucial for tasks such as topographic mapping, remote sensing data analysis, and precision surveying, as it enables the accurate mapping of image data to geographic coordinate systems. However, the traditional process of image geometric correction encounters several challenges, with the acquisition of high-quality ground control points (GCPs) being the most significant (Wang et al., 2012). Ground surveys in remote or difficult terrains are costly and time-consuming, and under certain conditions, such as extreme weather or political instability, obtaining GCPs in the field will be unfeasible (Baboo & Devi, 2011). These factors not only escalate project costs significantly but also may diminish the geometric correction accuracy due to insufficient GCPs, thus impacting the quality and reliability of the final application (Kardoulas et al., 1996).

Recently, advancements in image georeferencing through "cloud-control" photogrammetry (Zhang & Tao, 2017) using existing geo-encoded data as geometric control instead of filed GCPs have opened up possibilities for simplifying the geometric correction process in remote sensing imagery. Image georeferencing without GCPs utilizes the internal features of remote sensing images, like terrain and buildings, for precise geographical location estimation, significantly diminishing the reliance on external GCPs (Cai et al., 2020; Cao et al., 2019). By employing advanced image processing and machine learning algorithms, it enhances the automation and accuracy of geometric corrections, effectively reducing remote sensing data processing costs and making it well-suited for image analysis in extensive and inaccessible areas. "Cloud-control" photogrammetry leverages existing geospatial data for geometric control, thereby replacing traditional GCPs and facilitating efficient and intelligent image data processing through automated matching technology (Zhang & Tao, 2017; Cao et al, 2020). While these innovations have somewhat simplified the data processing and hold potential for cost reduction, their successful execution and the accuracy of the outcomes largely hinge on the development and meticulous implementation of advanced algorithms, particularly in complex terrains.

In this context, spaceborne lidar, offering close to centimeter-level vertical accuracy, has increasingly captured attention (Wang et al., 2018), introducing new possibilities for image geometric correction. Following the ICESat laser altimetry mission, NASA launched the ICESat-2 mission on September 15, 2018, aimed primarily at measuring changes in land ice elevation and sea-ice freeboard, as well as determining global vegetation canopy heights (Neumann et al., 2019; Liu et al., 2021). The Single-Photon LiDAR (SPL) onboard generates high-resolution laser point data, offering an unprecedented, detailed view of Earth's surface to the field of remote sensing. Specifically, the ATL03 dataset of ICESat-2 is especially noteworthy. It ensures a high density of laser points along the radar scanning direction, with a footprint spacing of 0.7 m (Markus et al., 2017). Furthermore, as illustrated in Figure 1 (Neumann et al., 2022), it features three groups of laser beams, each divided into strong and weak light (Markus et al., 2017), significantly enhancing surface coverage. Concurrently, numerous quality evaluation studies of ICESat-2 have demonstrated that its laser points can achieve the proclaimed decimeter-level vertical accuracy in most areas (Neuenschwander & Magruder, 2019; Zhao et al., 2021; Tian & Shan, 2021; Shang et al., 2022). This high-precision laser point data is not only crucial for monitoring polar ice caps and researching sea level changes, but also offers a new, high-quality, low-cost source of control points for the geometric correction of remote sensing images. Regrettably, most existing research

* Corresponding author

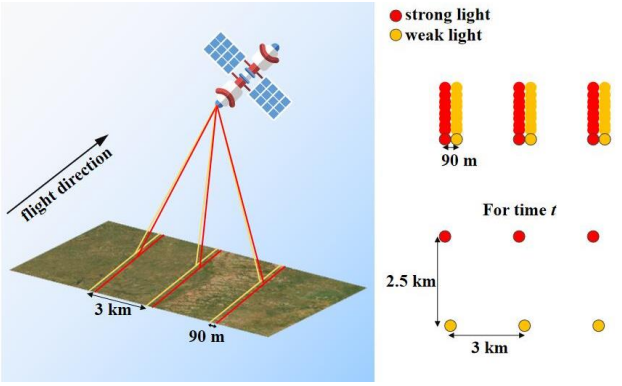


Figure 1. ICESat-2 ATLAS idealized beam and footprint pattern.

focuses solely on evaluating the vertical accuracy of ICESat-2 (Wang et al., 2021; Silva et al., 2021; Nandy et al., 2021) and its intended functions, overlooking its potential and practicality as a source of control points for image geometric correction. As Schenk's research mentioned, the planar accuracy of ICESat-2 is only 5-6 meters (Schenk, 2021), which means that the laser points can only be used as elevation control points (Wang et al., 2018). However, the concept of digital control photo (DCP) effectively addresses this issue (Zhang, 2023). A DCP is an image processed through aerial triangulation, featuring precise orientation parameters and dense control points, which can be used for accurate planar and elevation control of images. Combining laser points with images to form DCP is crucial for utilizing laser height measurement points in image correction.

This study presents a novel method for the geometric correction of remote sensing images using the ICESat-2 ATL03 data. By leveraging attribute labels and prior terrain data from ATL03 data products, we removed the noise and outlier points to obtain high-quality laser points suitable for reference data. The collected laser points are then quickly transferred to the reference image to obtain laser control points (LCPs) while simultaneously constructing the DCPs. The accuracy of image geometric correction is subsequently verified based on DCP. Our study comprehensively demonstrates the feasibility and significant accuracy advantages of implementing geometric correction with ICESat-2 laser point data through an in-depth introduction of the method, experimental design, and result analysis. It reveals the underutilized potential of ICESat-2 data in geometric correction of traditional remote sensing images and holds wide-ranging applications in future remote sensing endeavors, particularly in environmental monitoring, land use planning, and disaster management.

The remainder of this paper is organized as follows. Section 2 details the study areas and experimental data. Section 3 introduces the methods. Section 4 presents and discusses the results. Section 5 draws the conclusion.

## 2. The Study Areas and Experimental Data

### 2.1 Study Areas

The Hobart region of Australia is selected as the verification area. Located in southeastern Australia, Hobart, the capital of Tasmania, is uniquely positioned between the Queens and the River Derwent, boasting a rich blend of urban and natural landscapes. With a relatively mild average slope and close proximity to Mount Quinney, Hobart displays considerable terrain complexity. Choosing this area to validate the proposed method primarily considers two key factors. Firstly, assessing the geometric correction effect necessitates GCPs (Fraser and Hanley, 2015). Secondly, both imaging and laser data are time sensitive. Thus, the selection aims to choose an area with minimal surface changes, mitigating the disparity between the laser-collected ground objects and the image's corresponding targets.

We have chosen the sub-meter high-resolution GeoEye-1 satellite stereo images (Fraser & Ravanbakhsh, 2009) as the reference image, alongside LCPs, to construct DCP. The DCP encompasses both the object-space and image-space coordinates of the laser points, along with the entirety of the reference image. Figure 2(a) shows the GeoEye-1 satellite image, with the background image being the 1-meter resolution open-source orthophoto. In addition, IKONOS satellite images with a resolution of 1 meter were selected as validation data to evaluate the correction effect of the constructed DCP. The coverage of the selected images closely matches that of the GeoEye-1 images in this area, as shown in Figure 2(b).

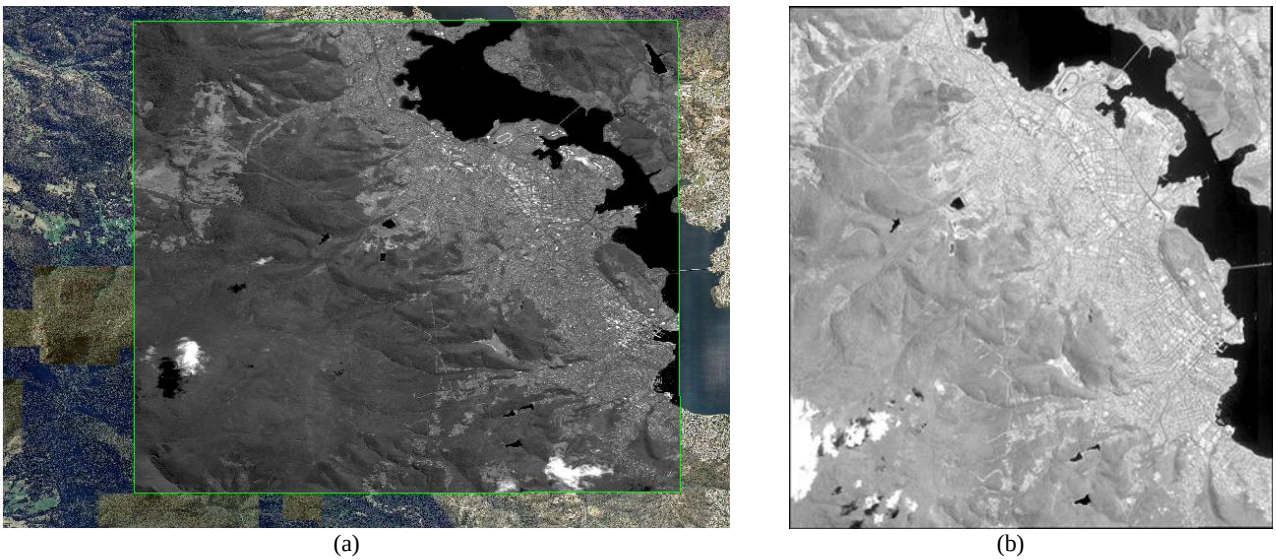

(a) (b)

Figure 2. Overview of the experimental dataset. (a) The GeoEye-1 image in Hobart, Australia and (b) the IKONOS satellite image utilized as verification data.

This contribution has been peer-reviewed. The double-blind peer-review was conducted on the basis of the full paper.
https://doi.org/10.5194/isprs-annals-X-3-2024-207-2024 | © Author(s) 2024. CC BY 4.0 License.

### 2.2 ATL03 Data

The ICESat-2 ATL03 data product offers globally geolocated photon data, detailing the exact latitude, longitude, and elevation for each received photon, organized by beam direction along the track. It categorizes photons into signal and background, as well as by surface type (e.g., land ice, sea ice, land, ocean), incorporating all geophysical corrections, including Earth tides and atmospheric delay (Neumann et al., 2022). For this study, we selected around seven periods of ATL03 data, each spanning three months (a full coverage period), within the GeoEye-1 image range. This resulted in a total of 21 track datasets, ensuring an adequate acquisition of laser points. Detailed data specifics are presented in Table 1.

| Year | Month | Track ID | Data File Name |
|---|---|---|---|
| 2022 | Jan | 337 | ATL03_20220113085316_03371409_006_01 |
| | | 375 | ATL03_20220115210324_03751413_006_01 |
| | Apr | 337 | ATL03_20220414043235_03371509_006_02 |
| | | 375 | ATL03_20220416164257_03751513_006_02 |
| | May | 317 | ATL03_20220515151923_08171513_006_01 |
| | Jun | 1282 | ATL03_20220615013655_12821509_006_01 |
| | Jul | 337 | ATL03_20220714001304_03371609_006_02 |
| | | 375 | ATL03_20220716122310_03751613_006_02 |
| | Sep | 1282 | ATL03_20220913211653_12821609_006_01 |
| | Oct | 337 | ATL03_20221012195252_03371709_006_01 |
| | | 375 | ATL03_20221015080259_03751713_006_01 |
| 2023 | Jan | 375 | ATL03_20230114034243_03751813_006_01 |
| | Feb | 817 | ATL03_20230212021848_08171813_006_01 |
| | Mar | 1282 | ATL03_20230314123618_12821809_006_01 |
| | Apr | 337 | ATL03_20230412111216_03371909_006_01 |
| | | 375 | ATL03_20230414232230_03751913_006_01 |
| | Jun | 1282 | ATL03_20230613081546_12821909_006_01 |
| | Jul | 337 | ATL03_20230712065139_03372009_006_01 |
| | | 375 | ATL03_20230714190145_03752013_006_01 |
| | Oct | 337 | ATL03_20231011023058_03372109_006_01 |
| | | 375 | ATL03_20231013144110_03752113_006_01 |

Table 1. The ATL03 dataset of the test area.

### 2.3 Other reference data

To further improve the screening of high-quality laser spots in ATL03, the global surface water and the global 30 m Shuttle Radar Topography Mission (SRTM) digital elevation model (DEM) are used as auxiliary reference data.

## 3. Study Design and Methods

### 3.1 Filtering of ATL03 laser points

The proposed method for generating LCPs utilizing ICESat-2 ATL03 dataset, involving two key steps: filtering laser points through attribute labels and using prior data for additional filtering.

#### 3.1.1 Filtering Based on Attribute Labels

Within the ICESat-2 ATL03 dataset, each photon's data is tagged with a signal_conf_ph attribute label. This label contains a 1×5 array indicating the photon's response to five surface types: land, ocean, sea ice, land ice, and inland water bodies, on a scale from -2 to 4, where 4 denotes the highest confidence. For the extraction of laser points aimed at elevation control, our filtering mechanism selectively included points with the utmost confidence in land type (specifically, a confidence level of 4) and excluded points where confidence levels fell below 2 for other land types, aiming to maximize the likelihood that selected points are land-based.

In addition, the ATL03 dataset includes a reference DEM identified by the dem_h label, along with a timestamp (delta_time label) for each photon's trajectory. This capability enables the calculation of the reference DEM elevation for each photon's location, derived through timestamp interpolation. By comparing this elevation to that of the photon, we further refine our laser point selection, excluding those exhibiting significant elevation discrepancies with the reference DEM. However, in practice, we found that the dem_h information coverage within ATL03 is incomplete, rendering its utility in filtering less evident. Consequently, this led us to incorporate prior data for an additional filter, beyond merely utilizing attribute labels as in the case with ATL08 data in numerous studies.

#### 3.1.2 Filtering Based on Prior Data

To address the issue of incomplete coverage associated with the dem_h label in ATL03 data, we utilized the 30 m SRTM DEM as a supplementary DEM. For the laser points filtered in Section 3.1.1, we calculated the elevation difference from SRTM DEM based on the longitude (lon_ph) and latitude (lat_ph) of the laser points, as well as their elevation (h_ph, the ellipsoidal height in the WGS84 coordinate system). This calculation is performed as follows:

$$\Delta H = |H_{ATL03} - H_{SRTM}| \quad (1)$$

According to Tian's study (Tian & Shan, 2021), the first and last 5% of photons with elevation differences were eliminated when evaluating photon accuracy. Therefore, we filtered out the top 10% of laser points by $\Delta H$ to remove as many erroneous points as possible. Although this approach inevitably removes some valid laser points on buildings, particularly high-rises, it effectively preserves high-quality laser points on bare ground to the greatest extent possible. Simultaneously, the prevalence of

high-rise buildings in Hobart is low, and such buildings will bring more environmental influences. Laser points on high-rise buildings are less effective than those on low-rise buildings and bare ground.

Furthermore, while the previously mentioned filtering based on the signal_conf_ph label can exclude most off-land laser points, the surface type grids do not perfectly tessellate the Earth's surface but have overlap on the order of tens of kilometers in most regions (Neumann et al., 2022). To mitigate this issue, we additionally employed a global water body mask file to filter out laser points located in water, ensuring that the remaining points predominantly fall on land.

By following the steps outlined above, we can efficiently extract high-quality laser points from ICESat-2 ATL03 dataset, thereby establishing a solid foundation for subsequent image geometric correction efforts.

### 3.2 Construction of DCP

Given the exceedingly large number of filtered ATL03 laser points, which surpass the quantity of GCPs gathered in the field, employing the traditional manual method to individually measure these points on the images for correction becomes time-consuming and inefficient. In this study, the obtained high-quality laser points can be projected into the image coordinate system of a high precision reference using the rational function model (RFM) (Wang et al., 2018). The RFM formula is as follows:

$$\begin{cases} r_n = \dfrac{Num_L(P_n, L_n, H_n)}{Den_L(P_n, L_n, H_n)} \\ c_n = \dfrac{Num_S(P_n, L_n, H_n)}{Den_S(P_n, L_n, H_n)} \end{cases} \quad (2)$$

Where $(P_n, L_n, H_n)$ represent regularized ground coordinates, $(c_n, r_n)$ denote regularized image coordinates. On this basis, combined with the RPC file of the image, the image coordinates of the ATL03 laser points can be calculated.

By applying the RFM, each laser point's geographical location is transformed into specific image coordinates. This step accounts for various geometric distortions in the imaging process and ensures the laser points are projected onto the reference image with exceptional accuracy. The combination of the laser points' geographical coordinates and their image coordinates with the high-precision reference image generates DCP. The DCP facilitates comprehensive geometric correction of the target image by combining image coordinates with the altimetry data of LCPs. In practical applications, the images and their RFM models we obtain are often not accurate enough. Therefore, before using the RFM model, we first perform geometric correction using open-source image data.

## 4. Experiments and discussions

### 4.1 Filtering of ICESat-2 ATL03

Within the coverage of the GeoEye-1 imagery, numerous laser points were extracted utilizing the proposed method. Using a grid with a spacing of 100 m in the latitude and longitude directions, 2163 laser points were extracted, whose distribution is shown in Figure 3.

As illustrated in Figure 3, within the GeoEye-1 imagery spanning approximately 15×15km, despite selecting seven coverage periods, the distribution of laser points was not as uniform as anticipated. Simultaneously, not every laser group displayed two distinct footprints (weak light and strong light); some exhibited only a single type, while others had one dense and one dispersed pattern. Considering the areas with sparse laser point extraction, it can be inferred that the collection efficiency of ICESat-2’s weak light beam is relatively inferior to that of its strong light beam. Moreover, the collection of single-photon LiDAR is significantly influenced by terrain, complicating the acquisition of high-quality laser points in rugged areas. Additionally, despite employing a water mask file to filter out laser points located in water bodies, some points within aquatic regions are inevitably retained. For this reason, the error points among the final laser points intended for geometric correction must be weighted and eliminated.

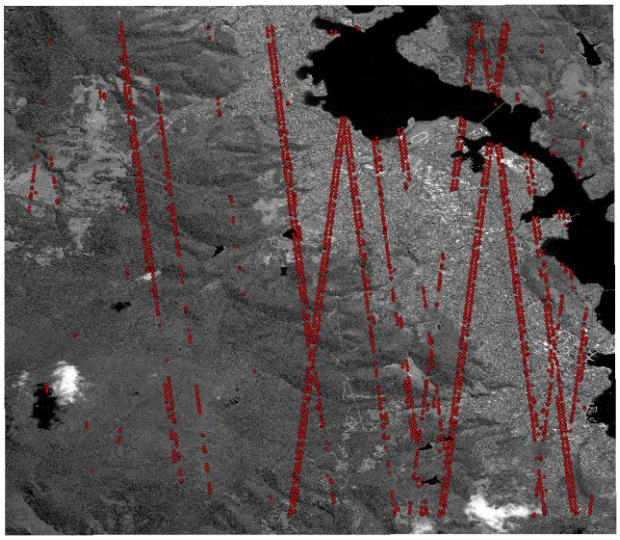

Figure 3. The distribution of extracted high-quality ATL03 laser points on the GeoEye-1 image.

### 4.2 Satellite images georeferencing

To evaluate the effectiveness of our proposed method for image georeferencing, we designed 4 distinct experiments. Concurrently, to facilitate precise geometric georeferencing of the satellite images, 17 GCPs were measured through ground surveying, as shown in Figure 4. The experiments were as follows: georeferencing (1) without GCPs, (2) using the reference DEM SRTM, (3) using 6 of 17 GCPs and (4) with the proposed DCP method. The first three experiments utilize well-known methods and serve merely as baselines for comparison; hence they will not be elaborated upon. Experiment (2) mainly demonstrates the elevation correction capabilities of SRTM DEM, laying the foundation for the introduction of our method.

In experiment (1), georeferencing was performed on the IKONOS image without GCPs, utilizing 17 GCPs as checkpoints for accuracy evaluation. The detailed results are shown in Table 2. The correction achieved meter-level precision, with horizontal and vertical root mean square errors (RSMEs) of 2.33 meters and 3.44 meters, respectively. Furthermore, the errors across the GCPs exhibited a random distribution pattern.

In experiment (4), georeferencing was conducted on the IKONOS image using the DCP we constructed, with 17 GCPs serving as checkpoints. As Figure 4 shows, because the IKONOS image range is slightly smaller than the Geo-Eye1 image, only 1979 LCPs (red dots in Figure 4a) out of the 2163 previously acquired can be used, and 341 LCPs were matched

successfully (green dots in Figure 4a), and finally the 278 LCPs in Figure 4b are used after adjustment. Table 3 displays the detailed outcomes, indicating that the correction achieved sub-meter accuracy, with horizontal and vertical RMSEs recorded at 0.36 meters and 0.26 meters, respectively. As illustrated in Figure 5, the accuracy significantly surpasses that of corrections performed without GCPs. The error distribution across each control point generally follows a random pattern, similar to experiment (1), evidencing that LCPs do not introduce significant local distortion to the image. Furthermore, Figure 5c clearly demonstrates that the DCP-based correction significantly enhances the vertical accuracy, but the error distribution is more scattered compared to the correction without GCPs. It is speculated that this is because the extracted LCPs contain poor quality points and erroneous points.

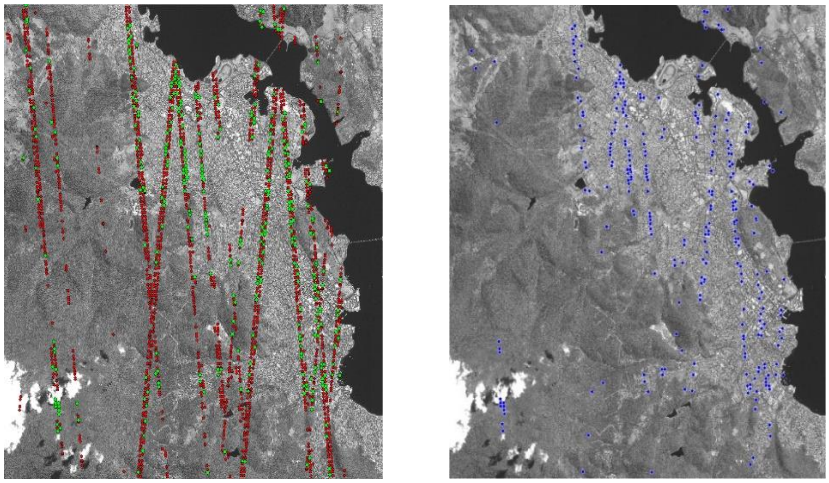

(a) (b)

Figure 4. (a) The distribution of LCPs within the IKONOS image range and successfully matched and (b) the distribution of LCPs finally used after adjustment elimination.

| GCP ID | $\Delta X$ | $\Delta Y$ | $\Delta Z$ |
|---|---|---|---|
| B5_04 | 2.00 | -1.20 | 3.44 |
| B1_01 | 1.82 | -1.15 | 3.14 |
| B6_20 | 2.18 | -1.16 | 3.82 |
| B9_05 | 2.21 | -0.99 | 4.08 |
| B2_04 | 2.05 | -1.25 | 3.24 |
| B1_02 | 1.89 | -0.91 | 3.40 |
| B3_10 | 2.27 | -1.13 | 3.73 |
| B5_06 | 2.18 | -1.18 | 3.97 |
| B4_03 | 1.71 | -1.53 | 2.81 |
| B5_01 | 2.53 | -1.14 | 3.44 |
| B5_02 | 2.42 | -1.33 | 3.41 |
| B9_16 | 2.08 | -1.12 | 3.78 |
| B7_07 | 1.54 | -1.14 | 2.70 |
| B7_10 | 1.29 | -0.96 | 3.24 |
| B8_01 | 2.04 | -1.12 | 3.25 |
| B5_11 | 1.87 | -1.33 | 3.66 |
| B1_10 | 1.96 | -0.88 | 2.97 |
| **RMSE** | **2.33** | | **3.44** |

Table 2. Georeferencing results of IKONOS image without ground control point (unit: m).

| GCP ID | $\Delta X$ | $\Delta Y$ | $\Delta Z$ |
|---|---|---|---|
| B5_04 | 0.14 | 0.91 | 0.32 |
| B1_01 | 0.01 | 0.68 | -0.45 |
| B6_20 | 0.26 | 1.00 | 0.74 |
| B9_05 | 0.38 | 1.29 | 1.37 |
| B2_04 | 0.21 | 0.70 | -0.17 |
| B1_02 | 0.07 | 0.91 | -0.26 |
| B3_10 | 0.25 | 0.73 | -0.11 |
| B5_06 | 0.27 | 0.85 | 0.62 |
| B4_03 | -0.03 | 0.47 | -0.36 |
| B5_01 | 0.60 | 0.88 | 0.05 |
| B5_02 | 0.52 | 0.76 | 0.20 |
| B9_16 | 0.29 | 1.17 | 1.13 |
| B7_07 | -0.04 | 1.01 | 0.01 |
| B7_10 | -0.29 | 1.20 | 0.57 |
| B8_01 | 0.31 | 1.10 | 0.55 |
| B5_11 | 0.05 | 0.74 | 0.52 |
| B1_10 | 0.25 | 0.89 | -0.63 |
| **ME** | **0.97** | | **0.59** |

Table 3. Georeferencing results of IKONOS image with DCP (unit: m).

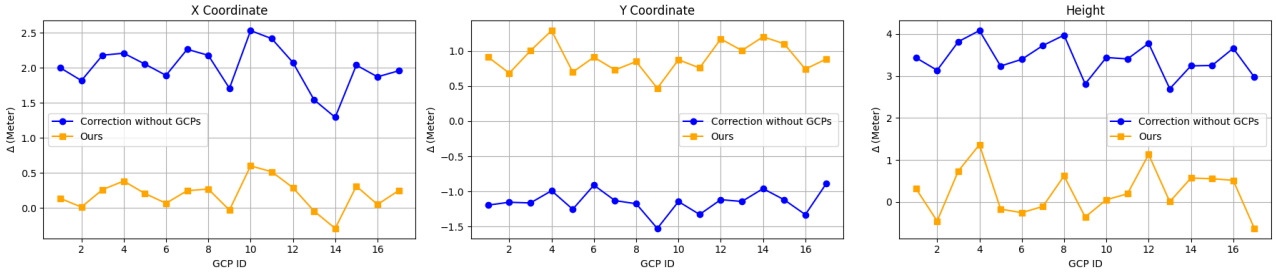


(a) (b) (c)

Figure 5. Geopositional errors of the 17 checkpoints in (a) X, (b) Y, and (c) Z directions after georeferencing without ground control points and with the proposed method.

Table 4 summarizes the final results of the four experimental groups, including the mean errors and RMSEs for each group, facilitating an in-depth analysis and comparison of performance across different experimental conditions. Experiments (2) and (3) implemented geometric corrections using the SRTM and 6 out of the 17 GCPs, respectively. Based on the results, the correction impact of SRTM on horizontal errors proves to be slightly better than correction without GCPs. From the mean error perspective, in comparison to experiment (1), there was a significant reduction from 3.42 meters to 0.64 meters, whereas the RMSE saw a modest improvement from 3.44 meters to 2.97 meters. There are reasons to question that due to the 30 m resolution of SRTM, which tends to smooth out most local elevations, thereby causing significant local distortion.

| Control data | Number of Checkpoints | RMSE | | | | Mean error | | |
|---|---|---|---|---|---|---|---|---|
| | | X | Y | XY | Z | X | Y | Z |
| No GCPs | 17 | 2.02 | 1.16 | 2.33 | 3.44 | 2.00 | -1.15 | 3.42 |
| SRTM | 17 | 2.02 | 1.16 | 2.33 | 2.97 | 2.00 | -1.15 | 0.64 |
| 6 GCPs | 11 | 0.19 | 0.14 | **0.23** | **0.25** | 0.03 | 0.02 | -0.03 |
| DCP | 17 | 0.28 | 0.92 | **0.97** | **0.59** | -0.19 | 0.90 | 0.24 |

Table 4. Experimental results of each group (unit: m).

In terms of RMSE, the geometric correction accuracy of our method still shows some differences from the horizontal and vertical errors of GCPs, with differences of 0.74 meters and 0.34 meters in horizontal and vertical, respectively. Although the difference in ME is slightly larger, both horizontal and vertical accuracies are at the sub-meter level. For the 1-meter resolution IKONOS image, the georeferencing accuracy of one pixel can already meet many industry needs. Overall, we find that the correction based on DCP performs well in the *X* and *Z* dimensions, and there is a certain improvement in the absolute correction amount in the Y direction. However, based on the inspection results of various GCPs, LCPs actually introduce errors that are completely opposite to those in the original images. This is worth further exploring in the future. This warrants further investigation to determine if there is an underlying systematic error in the horizontal georeferencing of ICESat-2 laser point data along the *Y* axis. Addressing this potential issue could enhance the accuracy and usability of ICESat-2 data for a broader range of applications.

Additionally, when a large local error occurs and the nearest GCP is far away, the local area is likely to remain uncorrected if relying solely on GCPs. In such cases, only the overall image correction accuracy can be guaranteed using GCPs. However, the DCP, which utilizes a large number of LCPs, can provide significant improvements in local correction despite not achieving the same overall accuracy as GCPs. Currently, the main limitation of the correction effect of DCP is the horizontal error of the laser height measurement points themselves, which results in a mismatch in elevation with the reference image. Furthermore, the accuracy of the reference image limits the use of laser height measurement points, and high-precision reference images s help accurately position these points on the image. In the future, with the continuous advancement of SPL, key indicators such as the horizontal accuracy of laser points are expected to improve continuously. Simultaneously, better reference image processing solutions and DCP-based geometric correction are anticipated to achieve better results.

## 5. Conclusion

This study underscores the efficacy of using ICESat-2 ATL03 dataset for the geometric correction of remote sensing images. Experiments were performed by constructing DCPs using the extracted ICESAT-2 ATL03 laser points and GeoEye-1 stereo images which were georeferenced by open-source orthophotos and DEMs as control, and then using the DCPs for georeferencing the IKONOS images. The results demonstrated a significant geometric accuracy improvement. Compared to the georeferencing method without GCPs, it improves horizontal accuracy from 2.33 meters to 0.97 meters and vertical accuracy from 3.44 meters to 0.59 meters for IKONOS.

The study not only highlights the untapped potential of ICESat-2 data for enhancing remote sensing applications but also offers a cost-effective, accurate, and efficient solution for georeferencing satellite images across diverse landscapes.

## Data Availability Statement

The IKONOS dataset and ground control points of Hobart area used in the study are available from https://www.isprs.org/data/ikonos_hobart/default.aspx.

## Acknowledgments

The authors would like to thank Imagery courtesy of Space Imaging LLC, GeoEye Inc., and Clive Fraser's research group at the University of Melbourne, Australia for making the IKONOS imagery, GeoEye-1 imagery, and ground control points in Hobart publicly available.

## References

Baboo, S. S., Devi, M. R., 2011. Geometric correction in recent high resolution satellite imagery: a case study in Coimbatore, Tamil Nadu. International *Journal of Computer Applications*, 14(1), 32–37.

Cai, Y., Ding, Y., Zhang, H., Xiu, J., & Liu, Z., 2020. Geo-Location Algorithm for Building Targets in Oblique Remote Sensing Images Based on Deep Learning and Height Estimation. *Remote Sensing*, 12, 2427.

Cao, H., Tao, P., Li, H., Shi, J., 2019. Bundle adjustment of satellite images based on an equivalent geometric sensor model with digital elevation model. *ISPRS Journal of Photogrammetry and Remote Sensing*, 156, 169-183.

Cao, H., Tao, P., Li, H., Zhang, Z., 2020. Using DEM as full controls in block adjustment of satellite imagery. *Acta Geodaetica et Cartographica Sinica*, 49(1), 79–91.

Dave, C. P., Joshi, R., Srivastava, S., 2015. A survey on geo metric correction of satellite imagery. *International Journal of Computer Applications*, 116(12): 24–27.

Fraser, C.S., Hanley, H.B., 2005. Bias-Compensated RPCs for Sensor Orientation of High-Resolution Satellite Imagery. *Photogrammetric Engineering & Remote Sensing*, 71(8): 909–915.

Fraser, C.S. and Ravanbakhsh, M., 2009. Georeferencing accuracy of GeoEye-1 imagery. *Photogrammetric engineering and remote sensing*, 75(6): 634-638.

Goncalves, H., Goncalves, J. A., Corte-Real, L., 2009. Measures for an Objective Evaluation of the Geometric Correction Process Quality. *IEEE Geoscience and Remote Sensing Letters*, 6(2), 292-296.

Kardoulas, N., Bird, A., Lawan, A., 1996. Geometric correction of SPOT and Landsat imagery: a comparison of map-and GPS-derived control points. *Photogrammetric Engineering and Remote Sensing*, 62(10), 1173–1177.

Liu, A., Cheng, X., Chen, Z., 2021. Performance evaluation of GEDI and ICESat-2 laser altimeter data for terrain and canopy height retrievals. *Remote Sensing of Environment*, 264, 112571.

Markus, T., Neumann, T., Martino, A., Abdalati, W., Brunt, K., Csatho, B., Farrell, S., Fricker, H., Gardner, A., Harding, D. et al., 2017. The Ice, Cloud, and land Elevation Satellite-2 (ICESat-2): science requirements, concept, and implementation. *Remote Sensing of Environment*, 190, 260–273.

Nandy, S., Srinet, R., Padalia, H., 2021. Mapping forest height and aboveground biomass by integrating ICESat-2, Sentinel-1 and Sentinel-2 data using Random Forest algorithm in northwest Himalayan foothills of India. *Geophysical Research Letters*, 48(14), e2021GL093799.

Neuenschwander, A. L., Magruder, L. A., 2019. Canopy and terrain height retrievals with ICESat-2: A first look. *Remote Sensing*, 11(14), 1721.

Neumann, T. A., A. Brenner, D. Hancock, J. Robbins, A. Gibbons, J. Lee, K. Harbeck, J. Saba, S. Luthcke, T. Rebold, 2022. Ice, Cloud, and Land Elevation Satellite (ICESat-2) Project Algorithm Theoretical Basis Document (ATBD) for Global Geolocated Photons ATL03, Version 6. ICESat-2 Project, DOI: 10.5067/GA5KCLJT7LOT.

Neumann, T. A., Martino, A. J., Markus, T., Bae, S., Bock, M. R., Brenner, A. C., Brunt, K. M., Cavanaugh, J., Fernandes, S. T., Hancock, D. W. et al., 2019. The Ice, Cloud, and Land Elevation Satellite–2 Mission: A global geolocated photon product derived from the advanced topographic laser altimeter system. *Remote Sensing of Environment*, 233, 111325.

Schenk, T., Csatho, B., Neumann, T., 2022. Assessment of ICESat-2’s Horizontal Accuracy Using Precisely Surveyed Terrains in McMurdo Dry Valleys, Antarctica. *IEEE Transactions on Geoscience and Remote Sensing*, 60, 4303811.

Shang, D., Zhang, Y., Dai, C., Ma, Q., Wang, Z., 2022. Extraction strategy for ICESat-2 elevation control points based on ATL08 product. *IEEE Transactions on Geoscience and Remote Sensing*, 60, 5705012.

Silva, C. A., Duncanson, L., Hancock, S., Neuenschwander, A., Thomas, N., Hofton, M., Fatoyinbo, L., Simard, M., Marshak, C. Z., Armston, J. et al., 2021. Fusing simulated GEDI, ICESat 2 and NISAR data for regional aboveground biomass mapping. *Remote Sensing of Environment*, 253, 112234.

Tian, X., Shan, J., 2021. Comprehensive evaluation of the ICESat-2 ATL08 terrain product. *IEEE Transactions on Geoscience and Remote Sensing*, 59(10), 8195–8209.

Wang, M., Wei, Y., Yang, B., Zhou, X., 2021. Extraction and analysis of global elevation control points from ICESat-2/ATLAS data. *Geomatics and Information Science of Wuhan University*, 46(2), 184-192.

Wang, J., Ge, Y., Heuvelink, G. B., Zhou, C., Brus, D., 2012. Effect of the sampling design of ground control points on the geometric correction of remotely sensed imagery. *International Journal of Applied Earth Observation and Geoinformation*, 18, 91-100.

Wang, J., Zhang, Y., Zhang, Z., Li, X., Tao, P., Song, M., 2018. ICESat laser points assisted block adjustment for mapping satellite-1 stereo imagery. *Acta Geodaetica et Cartographica Sinica*, 47(3), 359-369.

Zhang, Z., Duan, Y., Tao, P., 2023. From ground control point to digital control photo. *Geomatics and Information Science of Wuhan University*, 48(11), 1715-1723.

Zhang, Z., Tao, P., 2017. An overview on “cloud control” photogrammetry in big data era. *Acta Geodaetica et Cartographica Sinica*, 46(10), 1238-1248.

Zhao, Y., Wu, B., Shu, S., Yang, L., Wu, J., Yu, B., 2021. Evaluation of ICESat-2 ATL03/08 surface heights in urban environments using airborne LiDAR point cloud data. *IEEE Geoscience and Remote Sensing Letters*, 19, 1–5.